Journal of Taibah University for Science

ISSN: 1658-3655 (Online) Journal homepage: www.tandfonline.com/journals/tusc20

Improving microstructural properties, mechanical performance, and processability of flux-engineered stir cast boron carbide (B_4C)-reinforced AA6061 composites with K_2TiF_6 integration

Obinna Onyebuchi Barah, Ige Bori, Abdulrazak Jinadu Otaru & Hayat Khan

To cite this article: Obinna Onyebuchi Barah, Ige Bori, Abdulrazak Jinadu Otaru & Hayat Khan (2025) Improving microstructural properties, mechanical performance, and processability of flux-engineered stir cast boron carbide (B_4C)-reinforced AA6061 composites with K_2TiF_6 integration, Journal of Taibah University for Science, 19:1, 2590833, DOI: 10.1080/16583655.2025.2590833

To link to this article: https://doi.org/10.1080/16583655.2025.2590833

Published online: 30 Nov 2025.

JOURNAL OF TAIBAH UNIVERSITY FOR SCIENCE
2025, VOL. 19, NO. 1, 2590833
https://doi.org/10.1080/16583655.2025.2590833

RESEARCH ARTICLE

OPEN ACCESS Check for updates

Improving microstructural properties, mechanical performance, and processability of flux-engineered stir cast boron carbide (B_4C)-reinforced AA6061 composites with K_2TiF_6 integration

Obinna Onyebuchi Barah[a], Ige Bori[b], Abdulrazak Jinadu Otaru[c] and Hayat Khan[c]

[a]Department of Mechanical Engineering, School of Engineering and Applied Sciences, Kampala International University, Western Campus, Uganda; [b]Department of Mechanical Engineering, Kabale University, Kabale Municipality, Kabale, Uganda; [c]Chemical Engineering Department, College of Engineering, King Faisal University, Al Ahsa, Saudi Arabia

ABSTRACT

Flux-assisted stir casting of AA6061–B_4C is limited by incomplete wetting, oxide films, and porosity. This study optimizes the K_2TiF_6-assisted process, defining a minimal effective flux window (0.5–1.0 wt%) while holding melt (≈750 °C), stirring (≈600 rpm, 10 min), and mold temperature (≈250 °C) constant and varying B_4C (4–12 wt%) in a single, industry-style rig. SEM/EDS/XRD indicate near-uniform dispersion to 10 wt% and mild clustering at 12 wt%. Measurable performance gains. Measured as group means ± SD ($n = 3$), microhardness ($HV_{0.5}$) increased from 68 → 113 (+62%), and UTS rose from 142 → 215 MPa (+51.4%); porosity rose modestly (~1.5→3.5%). Rule-of-mixtures predictions reproduce the 4–12 wt% trend, supporting a mechanism in which low-dose K_2TiF_6 disrupts oxide films, enhances wetting, and improves load transfer. By quantifying a low-flux regime that limits Ti contamination and salt waste while delivering predictable structure–property outcomes, the work provides process-level guidance for scalable production of lightweight aluminum composites for weight-critical structural applications.

ARTICLE HISTORY
Received 12 August 2025
Revised 5 November 2025
Accepted 12 November 2025

KEYWORDS
Flux-assisted stir casting; Aluminum matrix composites; boron carbide (B_4C) reinforcement; K_2TiF_6 flux agent; circular economy

1 Introduction

The demand for lightweight, high-strength, and thermally stable materials is rising across various sectors, including aerospace, automotive, defense, building and construction, and energy. In these industries, critical design constraints include performance-to-weight ratio, fuel efficiency, high strength, and structural integrity [1–3]. In this context, aluminum matrix composites (AMCs) have gained significant attention for their ability to effectively combine the lightweight properties and processability of aluminum alloys with the mechanical strength and thermal stability of ceramic reinforcements [4,5]. As a result, these composites are increasingly used in applications such as structural panels, building materials, brake components, engine blocks, and ballistic systems.

Beyond single-ceramic systems, hybrid particulate routes have delivered concurrent gains in hardness and wear for Al cast alloys, for example A356 reinforced with fly ash/SiCp [6], AA6063 hybridized with $ZrSiO_4$+TiB_2 [7], and A356 with CaB_6 [7] highlighting the sensitivity of tribo-mechanical performance to reinforcement chemistry, morphology, and loading [8].

Boron carbide (B_4C) stands out among various ceramic reinforcements due to its exceptional properties, including ultra-high hardness (~30 GPa) [9,10], low density (2.52 g.cm^{-3}) [11], high elastic modulus,and excellent chemical and thermal stability. These characteristics make it particularly well-suited for applications requiring wear resistance,impact tolerance,and armor-grade performance [12,13]. Despite these advantages, the potential of B_4C-reinforced aluminum matrix composites (AMCs) remain largely untapped, primarily due to ongoing fabrication challenges. A significant obstacle to effective integration of B_4C is its poor wettability with molten aluminum, which results in non-uniform dispersion, interfacial debonding, and

CONTACT Obinna Onyebuchi Barah obinna.barah@kiu.ac.ug; Abdulrazak Jinadu Otaru aotaru@kfu.edu.sa

Article highlights

- This study presents a scalable and cost-effective method for fabricating B_4C-reinforced AA6061 aluminium matrix composites.
- Potassium titanium fluoride (K_2TiF_6) was used as the fluxing agent.
- This significantly improved particle wettability, interfacial bonding, and microstructural uniformity.
- Microstructural analyses (SEM, EDS, XRD) revealed optimal dispersion at up to 10 wt.% B_4C.
- Mechanical tests showed substantial enhancements in microhardness and ultimate tensile strength (UTS).
- A maximum UTS of 215 MPa was attained at 12 wt%.

particle agglomeration, particularly in liquid-state processing methods [10,14]. These interfacial issues impede efficient load transfer between the matrix and the reinforcement, thereby diminishing the anticipated mechanical benefits. Furthermore, if proper processing control is not maintained, the formation of undesirable intermetallic or residual porosity can further compromise the integrity of the composite. Stir casting is a popular method for producing aluminum matrix composites (AMC) in industrial settings due to its cost-effectiveness, relative simplicity, and scalability [15]. However, its effectiveness can be reduced when incorporating hard ceramic phases such as B_4C, unless specialized enhancements are applied. One effective strategy is to use wetting agents or fluxes to improve the thermodynamic affinity between the reinforcement and the molten metal.

Gu et al [12]. examined the effects of chlorinated salt flux in combination with an aluminum-boron (Al-B) master alloy on secondary Al-Si alloys. The fluxing treatment reportedly removed 89.9% of Mg, 68.9% of Ti, and 61.5% of V from the melt, refined the grain structure by 45.5%, and enhanced tensile strength by 28.7%. This demonstrates that the combined use of salt flux and master alloy effectively purifies the melt and significantly improves both microstructural control and mechanical performance. Kumar et al [13]. investigated activated tungsten inert gas (A-TIG) welding of AA6063-T6 using SiO_2-based flux. The application of flux resulted in noticeably increased weld penetration depth, narrower bead dimensions, and finer microstructures in the fusion zone. Mechanical testing revealed higher tensile strength and a ductile fracture mode in A-TIG samples compared to conventional TIG, which can largely be attributed to reduced oxide inclusions, refined grains, and enhanced weld pool dynamics during fusion.

Rana et al [14]. conducted a comparative investigation into the use of SiO_2 and TiO_2 active fluxes in A-TIG welding of nonferrous alloys. The study revealed that both oxides approximately doubled the penetration depth compared to conventional TIG, with SiO_2 achieving a 260% increase under specific conditions. Microstructural analysis indicated more defined ferrite formation and pronounced arc constriction effects, leading to deeper weld profiles, narrower bead widths, refined grain structures, and improved hardness. Additionally, a review focusing on solid salt flux strategies in molten aluminum recycling [15,16] highlighted that well-composed chloride- and fluoride-based salt fluxes protect the melt from oxidation, facilitate impurity removal, and assist in dross treatment. The physical and chemical characteristics of these fluxes, such as density, fluidity, wettability, and melting point, were shown to strongly correlate with enhanced metal cleanliness and higher recovery rates during processing. Collectively, these studies emphasize how both chemical fluxes (chlorinated salts, ceramic oxides) and master-alloy inoculants (Al-B) improve metal quality by facilitating impurity removal and promoting grain refinement. Recent stir–ultrasonic–squeeze casting routes for AA6061 hybrid nanocomposites report notable gains in hardness and tribology due to cavitation-assisted dispersion and pressure solidification. However, these multi-step routes increase equipment and energy demands, and a quantified low-flux window for simpler flux-assisted stir casting has not been established [16].

Potassium titanium fluoride (K_2TiF_6) improves wettability by modifying surface energy and disrupting oxide layers in aluminum melts [17,18], yet a quantitative, low-dose process window and its coupled effect on dispersion, porosity, and properties across a controlled B_4C sweep remain insufficiently defined under consistent, industry-style stir-casting conditions. This study therefore aims to (i) establish the minimal effective K_2TiF_6 window (0.5–1.0 wt%), (ii) map structure–property relations for 4–12 wt% B_4C (dispersion/porosity → $HV_{0.5}$/UTS), and (iii) benchmark observations against rule-of-mixtures predictions. Hypotheses: (H1) low-dose K_2TiF_6 enhances wetting and reduces porosity, increasing hardness and UTS without over-fluxing; (H2) an optimum B_4C loading (≈10–12 wt%) balances strengthening and dispersion; (H3) ROM trends will agree with measurements within experimental scatter. Expected outcomes include statistically supported gains in $HV_{0.5}$ and UTS relative to the unreinforced control, near-uniform dispersion up to 10 wt% with mild clustering at 12 wt%, and process-level guidance for scalable, lightweight, wear- and impact-resistant aluminum composites.

2 Research materials, methods and characterization

The operational methodology used in this study begins with the selection of raw materials and continues through to the characterization and analysis of experimental data, as illustrated in Figure 1 below. A brief justification for the choice of potassium titanium fluoride (K_2TiF_6) and detailed experimental procedures are provided below:

2.1 Cost–efficiency and comparative justification of K_2TiF_6

The choice of potassium titanium fluoride (K_2TiF_6) not only enhances wettability but also offers practical economic benefits. Compared to commonly used fluxes like sodium cryolite (Na_3AlF_6), K_2TiF_6 demonstrates superior thermochemical reactivity, leading to more effective disruption of oxide layers and improved

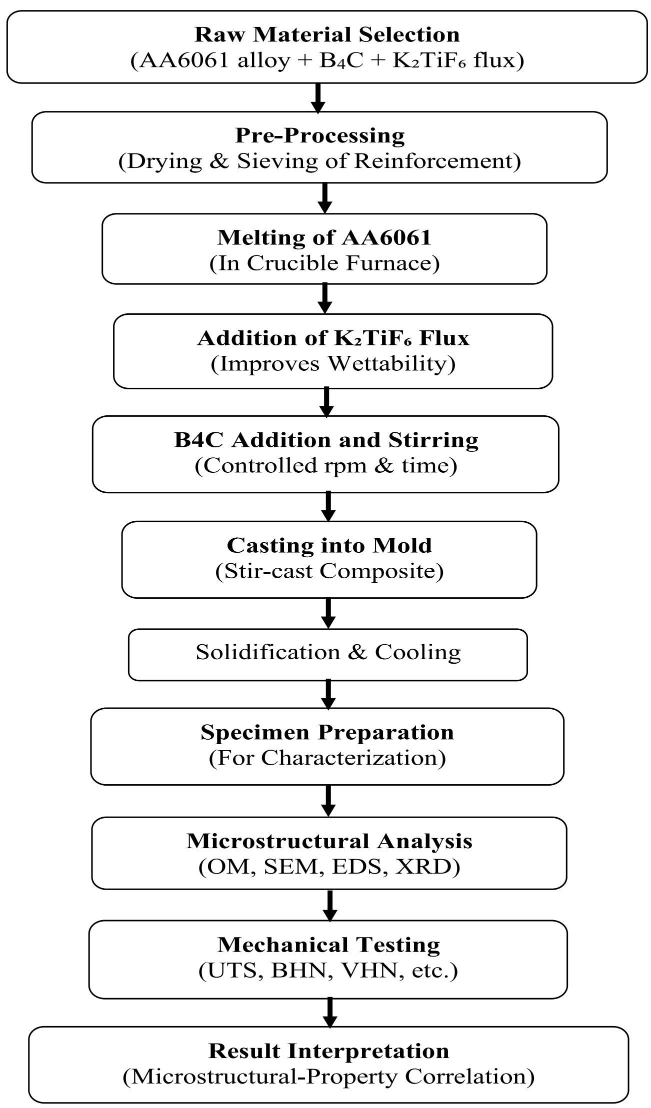

Figure 1. Flow diagram illustrating the sequence of fabrication and characterization for AA6061-B_4C composites produced via flux-assisted stir casting using K_2TiF_6.

interfacial bonding at lower concentrations (typically 0.5–1 wt.%). While its per-unit cost is somewhat higher, the need for reduced dosage and better reinforcement dispersion results in lower overall material usage and fewer casting defects, ultimately leading to cost savings in production cycles. Previous studies [19,20] have indicated that Na_3AlF_6 often underperforms in ceramic-reinforced systems, such as B_4C, due to limited fluoride mobility and weaker interfacial activation. Therefore, K_2TiF_6 is a technically and economically sound choice for ensuring consistent composite quality in industrial stir casting applications.

2.2 Materials

The matrix material selected for this study was AA6061 aluminum alloy, recognized for its outstanding mechanical strength, corrosion resistance, and weldability, making it suitable for structural and transportation applications. The alloy was sourced in ingot form from a certified industrial supplier and met the compositional standards outlined in ASTM B221. Its nominal chemical composition by weight (%) was as follows: Al–97.9, Mg–1.0, Si–0.6, Cu–0.28, Cr–0.2, with trace elements present at levels below 0.1%. Boron carbide (B_4C) powder was chosen as the ceramic reinforcement due to its ultra-high hardness, low density, high modulus of elasticity, and chemical inertness. The B_4C powder was purchased from the open market, with a reported purity exceeding 98%, a particle size of 40–50 µm, and an angular morphology, which was subsequently confirmed through SEM imaging. To minimize moisture absorption and thermal shock when introduced into the melt, the B_4C particles were preheated to 250 °C for 1 hour in a muffle furnace. Potassium titanium fluoride (K_2TiF_6) was added as a fluxing agent to address the inherent wettability challenges of B_4C in molten aluminum and to promote uniform phase distribution. Potassium titanium fluoride (K_2TiF_6) is known to disrupt surface oxides and reduce interfacial energy, thereby enhancing wetting and bonding between the matrix and reinforcement phases [21].

2.3 Composite fabrication via modified casting

Figure 2 illustrates a precision-engineered modified bottom-pour resistance-heated stir casting system specifically optimized to produce AA6061-B_4C composites. In this apparatus, AA6061 alloy ingots are

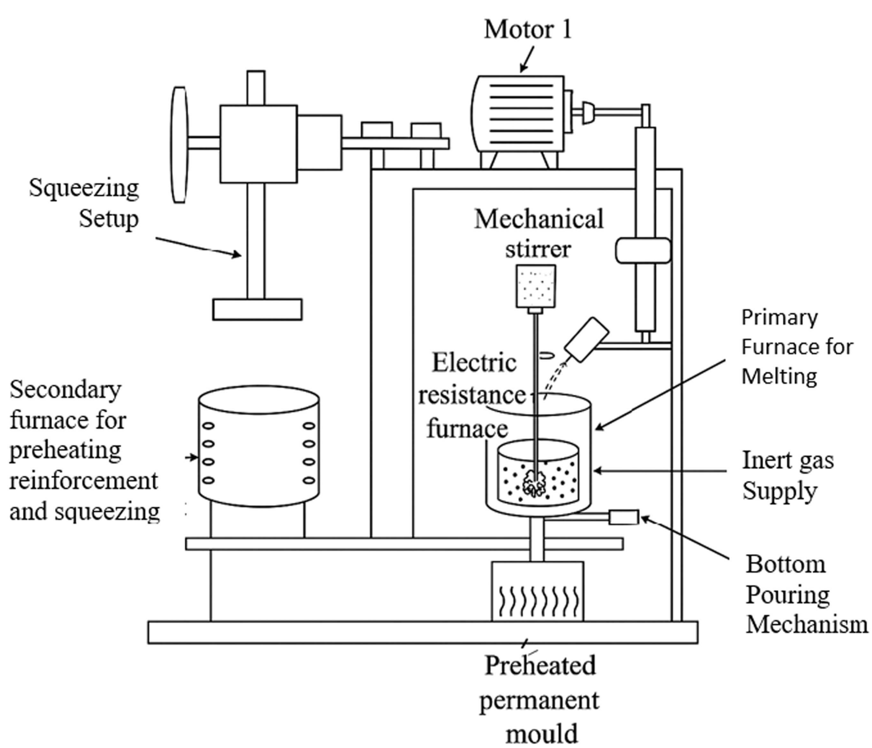

Figure 2. Schematic diagram of a modified stir casting setup, highlighting the key components.

melted and maintained at 750 ± 5 °C in an argon-shielded electric-resistance furnace, ensuring thermal equilibrium and preventing oxidation. AA6061 alloy ingots were melted and maintained at 750 ± 5 °C in an argon-shielded electric-resistance furnace, ensuring thermal equilibrium and preventing oxidation. Argon flow was maintained at ~5 L min^{-1}; no oxide skin was observed after a 5-min hold, and oxygen content in the furnace atmosphere remained below 0.02 vol % (≈200 ppm O_2) throughout the melt stage, confirming effective shielding.

Flux dissolution verification. After introducing 0.5 wt.% K_2TiF_6 at 750 ± 5 °C, the melt was stirred for 2 min with a zirconia-coated impeller; dissolution was considered complete when no undissolved residue or scum was visible and the surface cleared. Preheated B_4C particles are then introduced via a controlled mechanism into the vortex and stirred at 600 rpm for 10 minutes, promoting uniform dispersion, effective wetting, and minimizing clustering.

Rationale for parameter selection: 600 rpm provides an impeller tip speed $u_t = \pi DN$, in the vigorous macromixing regime (for a 40–50 mm impeller, $u_t = 1.3 - 1.6\ ms^{-1}$), yielding high Reynolds numbers suitable for particle entrainment while avoiding excessive surface draw-down and gas entrainment; a 10-minute dwell corresponds to multiple circulation turnover times, sufficient to reach thermal and concentration homogeneity for 0–12 wt.% solids at 750 °C without overexposing the melt to the free surface. These settings therefore balance entrainment efficacy against porosity risk and were adopted for all reported batches.

The composite melt is bottom-poured into steel molds preheated to 200 °C, which reduces turbulence, porosity, and thermal gradients. Key differences from stir–ultrasonic–squeeze protocols [22–24] include the absence of ultrasonic cavitation and squeeze pressure; wetting is instead promoted via K_2TiF_6-mediated oxide disruption at low dose. An optional squeeze casting step may further densify the composite before solidification. Batches containing 4, 6, 8, 10, and 12 wt.% B_4C were produced, cooled under ambient conditions, sectioned, and prepared for microstructural and mechanical characterization.

This methodology closely aligns with recent studies, which indicate that bottom-pour stir casting under inert gas has effectively produced Al–TiC composites with significantly reduced oxide inclusions and improved wear resistance [22]. Modified rigs using bottom pouring have also shown enhanced homogeneity and improved mechanical properties in Al–SiC systems. Furthermore, the integration of ultrasonic-assisted stirring with inert-gas protection and bottom pouring in Al6061–CuO composites has resulted in superior particle distribution, low porosity, and strong microstructures [22]**.** Comprehensive reviews highlight that configurations combining electromagnetic or ultrasonic stirring, bottom pouring, and squeeze casting are regarded as the industry standard for maximizing composite quality in advanced MMCs [23]. These findings confirm that the design and operation of Figure 2 represent state-of-the-art stir casting methodology, incorporating multispectral enhancements to optimize microstructure and mechanical performance.

2.4 Characterization techniques

Specimens were sectioned from the castings, ground using 240–1200 grit SiC, polished with a 0.3 µm alumina suspension, and etched with Keller's reagent to reveal grain boundaries. Microstructural morphology and particle distribution were assessed through optical microscopy and scanning electron microscopy (SEM) using a JEOL JSM–6490 (JEOL Ltd., Tokyo, Japan). Energy-dispersive X-ray spectroscopy (EDS) was employed to evaluate chemical uniformity across the matrix and reinforcement regions. X-ray diffraction (using a PANalytical X'Pert PRO with Cu-Kα radiation, 2θ = 10°–80°) confirmed the presence of B_4C, detected interfacial reaction products, and tracked changes in crystallinity with varying reinforcement. EDS point and line scans were utilized to investigate the interfaces between particles and the matrix, as well as potential elemental diffusion.

2.5 Phase and interfacial chemistry (XRD and SEM-EDS)

Phase and interfacial characterization were performed by X-ray diffraction (XRD) and SEM–EDS to evaluate reactions associated with the K_2TiF_6 flux. XRD used Cu Kα radiation ($\lambda = 1.5406$ Å), 2θ = 20–90°, step = 0.02°, counting time ≥1 s/step. Reference patterns were Al (FCC), B_4C, TiC, Al_3Ti, and AlTi (ICDD PDF). Backgrounds were fit with a polynomial; phase matching required ≥3 peaks. The nominal limit of detection (LoD) for minority phases was estimated from peak-to-background ratios.

SEM–EDS (15–20 kV; 10–12 mm WD) examined K_2TiF_6 residues and Al/B_4C interfaces. For each composition we acquired (i) area maps across Al–B_4C interfaces and (ii) line scans across individual interfaces.

2.6 Mechanical testing

Mechanical characterization was performed to quantify the strengthening effects of B_4C reinforcement on the AA6061 matrix. The evaluation focused on two key metrics: ultimate tensile strength (UTS), which measures the composite's load-bearing capacity under uniaxial stress, and hardness, which indicates resistance to localized plastic deformation. Together, these properties offer a comprehensive assessment of both bulk and surface-level mechanical performance. Standardized testing protocols were followed to ensure reproducibility and comparability across different levels of reinforcement. The results were analyzed in relation to microstructural features, including particle dispersion, porosity, and interfacial bonding. Figure 3 presents images illustrating the cast specimen and its labeling, along with a schematic representation of the micro-tensile test specimen featuring a dog-bone geometry. The following is a detailed outline of the experimental procedure for the tensile and hardness testing conducted in this study:

2.6.1 Tensile testing protocol (macro-scale mechanical response)

A uniaxial tensile test was conducted in accordance with the ASTM E8/E8M−24 standard to assess the load-bearing capacity and ductile response of the fabricated AA6061-B_4C composites. Sub-sized dog-bone specimens were machined from the as-cast ingots using wire EDM to minimize residual stresses and dimensional distortion. The gauge length and cross-sectional area adhered to standard specifications, ensuring comparability and repeatability across different reinforcement levels. The test was performed using a servo-hydraulic Instron 5980 (Instron, Norwood, MA, U.S.A.) universal testing machine equipped with a 100 kN load cell and controlled via Bluehill Universal software. A constant crosshead speed of 2 mm/min was applied under displacement control to maintain quasi-static loading conditions.

To address potential variability from particle clustering or local porosity, three replicate specimens were tested for each composition, and the resulting stress–strain curves were analyzed to determine the ultimate tensile strength (UTS). Strain measurements were taken using the machine's built-in extensometer to

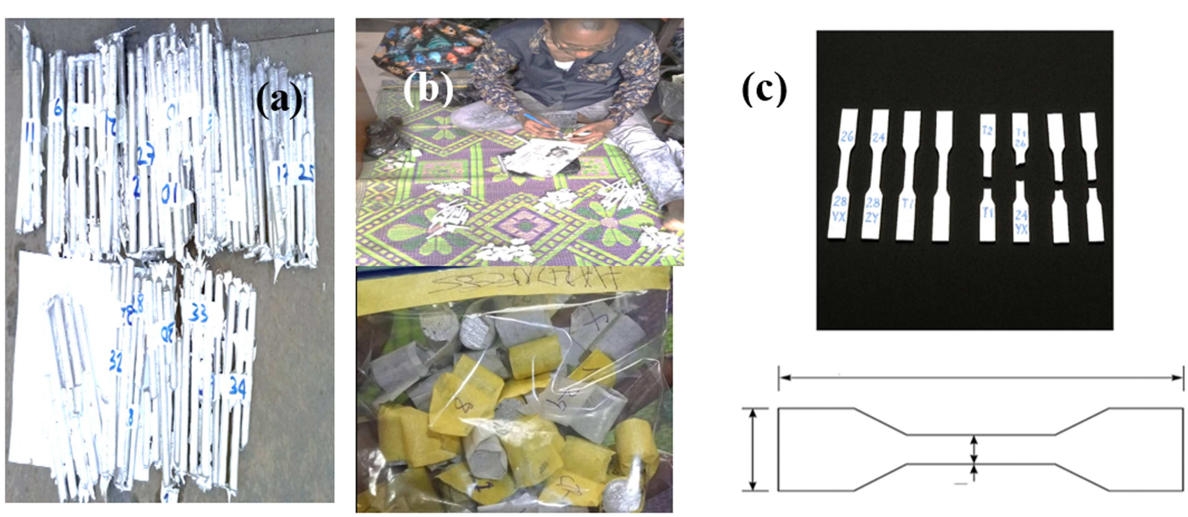

Figure 3. (a) Cast specimen; (b) specimen labeling; (c) AA6061–B_4C composite specimens, along with a schematic diagram of a micro-tensile test specimen featuring a dog-bone geometry.

ensure accurate tracking of elongation. The mechanical response of the composites was evaluated based on:

1. Load transfer efficiency from the ductile matrix to the rigid B_4C particles,
2. Interfacial bonding strength enhanced by flux-assisted wetting,
3. The impact of reinforcement dispersion uniformity on local strain distribution and failure modes.

The observed UTS trends provided valuable insights into the reinforcement threshold, indicating the point at which mechanical benefits either plateaued or were compromised by defects caused by agglomeration.

2.6.2 Hardness testing methods (micro/macro indentation resistance)

Two complementary indentation techniques were used to assess the surface-level and bulk hardness of the composites: Vickers microhardness testing and Brinell macrohardness testing, as described below. Microhardness was measured using a Shimadzu HMV (Shimadzu Corp., Kyoto, Japan) Vickers tester equipped with a diamond indenter angled at 136° between its opposing faces. Indentations were created under a load of 500 g with a dwell time of approximately 15 seconds. The Vickers hardness value (HV) was calculated using Equation 1:

$$HV = \frac{\left[2P\sin\left(\frac{\alpha}{2}\right)\right]}{D^2} \tag{1}$$

where P represents the applied load (kgf), α is the angle between the indenter faces (136°), and D is the mean diagonal of the indentation (mm). This method only probes a shallow surface depth, making the measured hardness sensitive to localized features such as porosity, clustering, or phase inhomogeneity—an important consideration in multi-phase systems like these composites.

The macrohardness was measured in accordance with ASTM E10–23 using a 10 mm diameter steel ball under a load of 500 g applied for approximately 20 seconds. The Brinell Hardness Number (BHN) was calculated using Equation 2:

$$BHN = \frac{P}{\frac{\pi D}{2}\left[D - \sqrt{D^2 - d^2}\right]} \tag{2}$$

where P is the applied load (kg), D is the ball diameter (mm), and d is the indentation diameter (mm). This technique samples a greater depth and volume, providing a more representative measure of the material's bulk response, which is less influenced by surface irregularities.

2.6.3 Density and porosity tests

The experimental density of the composites was determined using Archimedes' principle, following ASTM B962–23. Samples were weighed both in air and while submerged in distilled water. The density was then calculated and is expressed in Equation (3):

$$\rho_{experimental} = \frac{W_{air}}{W_{air} - W_{water}} * \rho_{water} \tag{3}$$

W_{air} = weight of the specimen in air.
W_{water} = weight of the specimen in water.
ρ_{water} = density of distilled water at ambient temperature (typically 0.9975 $g.cm^{-3}$ at 25 °C).

The theoretical density of the composite was calculated using the rule of mixtures in Equation 4:

$$\rho_{theoritical} = \left(\frac{W_m}{\rho_m} + \frac{W_r}{\rho_r}\right)^{-1} \tag{4}$$

W_m *and* W_r represent the weight fractions of the matrix (AA6061) and reinforcement (B_4C), respectively. ρ_m *and* ρ_r represent the densities of the matrix (2.70 $g.cm^{-3}$ for AA6061) and B_4C (2.52 $g.cm^{-3}$). The percentage porosity was calculated to evaluate the volumetric content of internal voids or defects using Equation (5):

$$Porosity(\%) = \left(\frac{\rho_{theoritical} - \rho_{experimental}}{\rho_{theoritical}}\right) * 100 \tag{5}$$

This metric offers insight into the densification quality of the fabricated composites. Lower porosity signifies better wettability, less entrapped gas, and more effective particle integration during casting. The enhanced microstructure and dispersion quality observed at 4–10 wt.% B_4C can be directly linked to the controlled stir casting regime and flux treatment detailed in Table 1, which optimized particle incorporation and matrix bonding.

3 Discussion of results

This section interprets the measured responses by linking flux-enabled wetting, particle dispersion/porosity, and the resulting mechanical behavior, rather than restating observations.

3.1 Microstructural and particle dispersion

Flux dose, rather than particle loading alone, governed dispersion quality up to a threshold of ~10 wt.% B_4C. Low-dose K_2TiF_6 (0.5–1.0 wt.%) disrupts native oxide films and reduces the particle–melt contact angle, enabling capillary infiltration of B_4C into the vortex and suppressing surface rafting [25,26]. Accordingly, at 4–6 wt.%, optical and SEM micrographs (Figures 4, 5, and 7) show homogeneous particle fields within a refined dendritic matrix, establishing semi-continuous load paths and minimizing local strain gradients. At 8 wt.%, dispersion remains broadly uniform but incipient clustering appears along grain boundaries as the effective suspension viscosity rises and inter-particle encounters increase. By 12 wt.%, agglomeration and partial sedimentation are evident: elevated particle volume fraction increases viscosity and reduces mobility during stirring; residual surface films promote particle bridging; and Stokes settling becomes competitive during quiescent intervals. These features introduce stress concentrators and microstructural heterogeneity, anticipating the observed balance between strength gains and ductility loss at higher loadings. Under the present conditions (~750 °C melt; ~600 rpm, 10 min; steel mold ~250 °C), the flux-enabled wetting maintained near-uniform dispersion up to 10 wt.%. Quantitative dispersion analysis was carried out on the micrographs in Figures 4 and 5 using a 15 × 15 grid segmentation and threshold-based particle recognition in ImageJ. The area fraction standard deviation (σ_a) across ten fields per composition served as the uniformity index. σ_a remained ≤4.8% up to 10 wt.% B_4C, indicating statistically uniform particle distribution, but increased sharply to 11.2% at 12 wt.% B_4C due to localized agglomeration. The mean inter-particle spacing ($\bar{\lambda}$), derived from nearest-neighbor centroid mapping, decreased monotonically from 28.4 µm (4 wt.%) to 16.1 µm (10 wt.%), with a coefficient of variation below 0.15, confirming homogeneous reinforcement dispersion within this range. These quantitative metrics substantiate the qualitative

Table 1. Processing parameters for stir casting of B_4C–AA6061 composites.

Parameter	Value/Description
Matrix Alloy	AA6061 (T6 condition)
Reinforcement	B_4C (particle size ~20 µm)
B_4C Content	0–12 wt.%
Melting Temperature	750 °C
Stirring Speed	600 rpm
Stirring Time	10 minutes
Flux Treatment	K_2TiF_6, 1 wt.% of melt
Casting Method	Gravity-assisted stir casting
Mold Type	Preheated steel mold (250 °C)
Cooling Method	Ambient air cooling

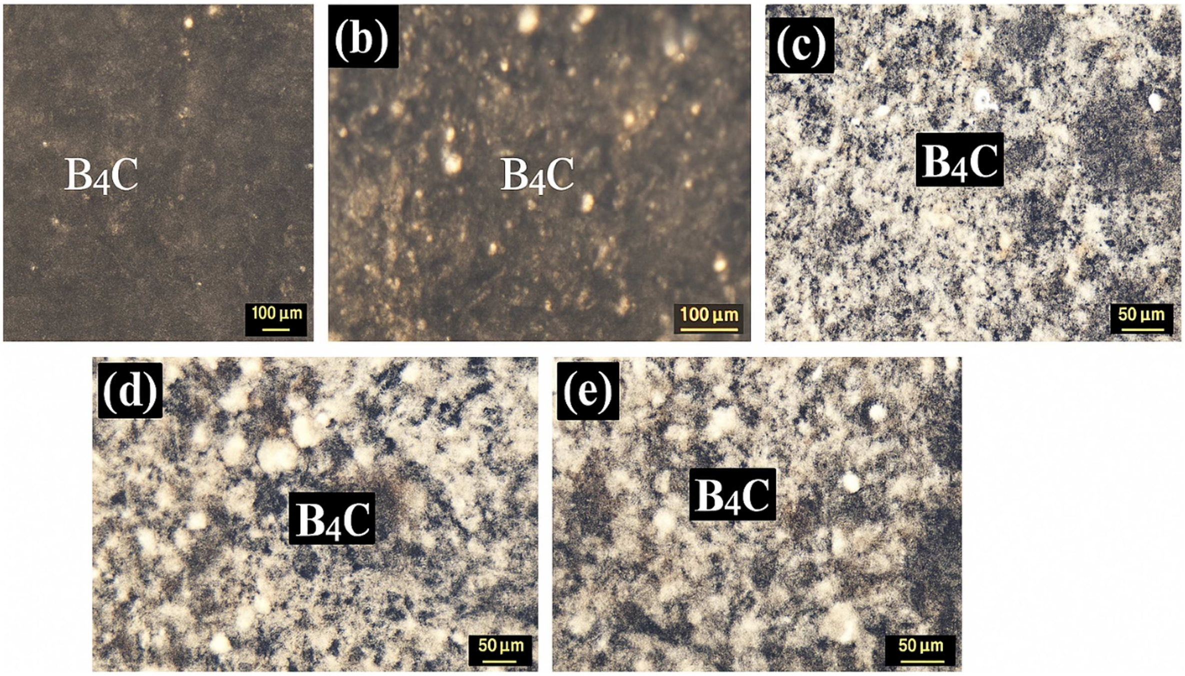

Figure 4. Optical micrographs showing B_4C particle dispersion in Al 6061–B_4C composites at different reinforcement contents: (a) 0 wt.% B_4C (base alloy), (b) 4 wt.%, (c) 8 wt.%, (d) 10 wt.%, and (e) 12 wt.% B_4C. Scale bars: (a,b) 100 µm, (c–e) 50 µm. Magnifications: (a,b) 200×, (c–e) 500×. Uniform particle distribution is maintained up to 10 wt.% B_4C, while localized clustering appears at 12 wt.%.

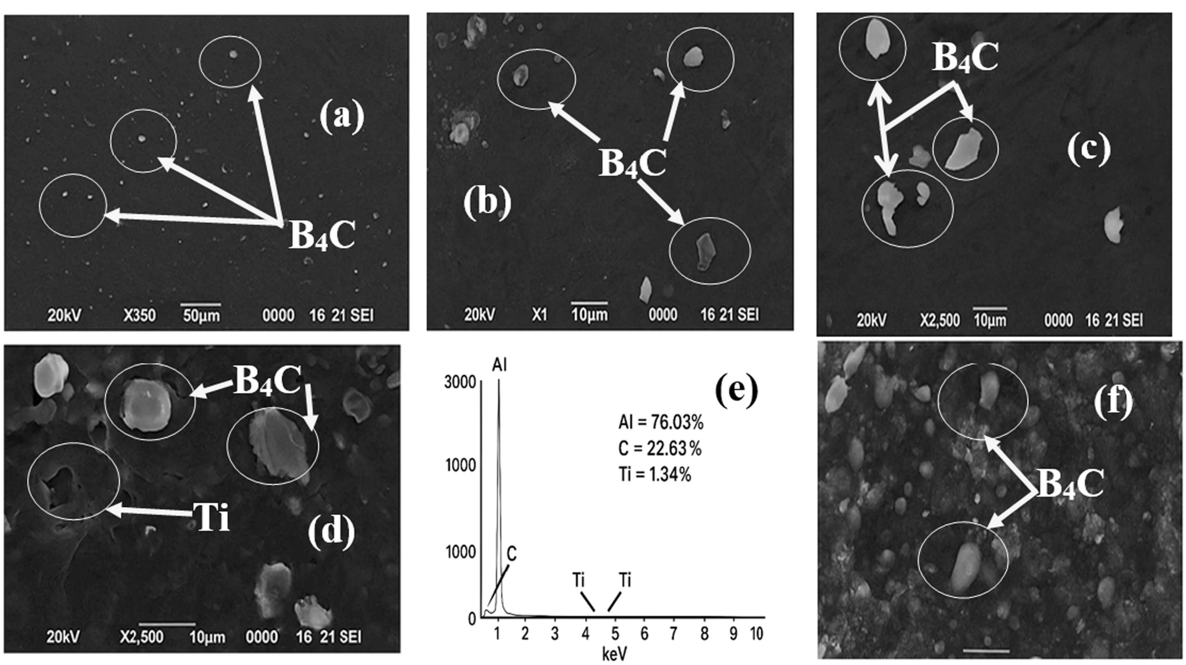

Figure 5. SEM micrographs of cast AA6061–B_4C composites at reinforcement levels of (a) 4%, (b) 6%, (c) 8%, (d) 10%, and (f) 12%. Plot (e) displays the corresponding EDAX spectrum for the 10% B_4C sample.

observation that microstructural uniformity is maintained up to 10 wt.% B_4C, beyond which clustering and porosity become evident (Figure 6). Beyond this point, additional reinforcement delivered diminishing returns because clustering-associated porosity and strain localization offset the benefits of higher rigid-particle content. The data therefore identify ≈10 wt.% as a process-defined dispersion limit for flux-assisted

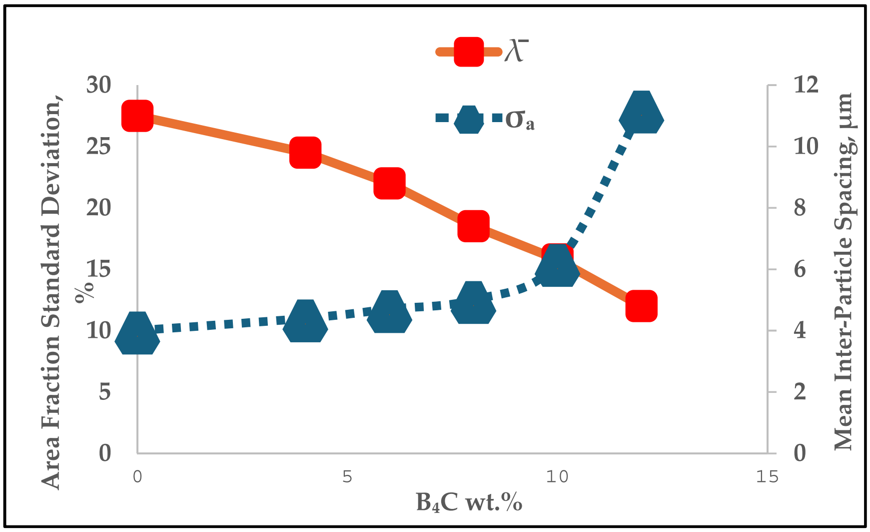

Figure 6. Quantitative dispersion metrics of Al–B_4C composites. Area-fraction SD (σ_a) and mean inter-particle spacing ($\bar{\lambda}$) vs. B_4C content. σ_a stays ≤4.8% through 10 wt.% (uniform dispersion) but jumps to 11.2% at 12 wt.% (clustering). $\bar{\lambda}$ falls from 27.5 to 15.8 µm, confirming tighter, effective dispersion up to 10 wt.%.

stir casting, set primarily by wettability and flow (flux + hydrodynamics) rather than by chemistry or nominal loading alone.

3.2 Interfacial behavior, phase stability and XRD data

The SEM micrographs in Figure 5 reveal that the interfaces between the B_4C particles and the aluminum matrix are tightly bonded, particularly in the flux-treated samples. Energy dispersive spectroscopy (EDS) line scans show smooth compositional transitions, with no evidence of oxygen-rich interfaces or voids. This strongly indicates that K_2TiF_6 effectively deoxidizes the surfaces of both the matrix and the reinforcement, enhancing the physicochemical affinity at the interface [26–28].

Figure 8 shows X-ray diffraction (XRD) patterns that confirm the presence of B_4C peaks and the absence of harmful intermetallic compounds, such as Al_4C_3, which are typically found in unmodified stir casting of ceramic reinforcements in aluminum alloys. The retention of B_4C's crystalline phase and the lack of brittle intermediates support the thermodynamic favorability of the flux-assisted process conducted at 750 °C. In contrast to flux-free stir casting methods reported in studies [29,30], which often result in high porosity and poor wettability, this study highlights that fluxing agent are essential for the effective incorporation and stability of ceramic reinforcements like B_4C.

3.3 Phase evolution and interfacial chemistry

XRD. Diffraction patterns (Figure 9d) are dominated by Al and B_4C peaks. Weak reflections indexed to TiC and Al–Ti intermetallics (Al_3Ti/AlTi) occur near the LoD, indicating at most trace reaction products associated with K_2TiF_6–assisted processing rather than bulk phase formation.

SEM–EDS. Micrographs (Figure 9a,b) show residual K_2TiF_6 particles at/near Al–B_4C interfaces (50 µm scale). Corresponding EDS maps/points reveal localized Ti and F enrichment confined to these regions, with negligible Ti/F in the surrounding Al matrix, evidence that not all K_2TiF_6 dissolved, and any Ti transfer was spatially limited. The particulate morphology shown in Figure 9c (100 µm scale) is consistent with agglomerated precursor/residual flux fragments.

Implication. Under the present conditions, K_2TiF_6 primarily aids wetting/oxide removal; only trace Ti-bearing products are detectable by XRD, and Ti/F enrichment is localized, not matrix-wide.

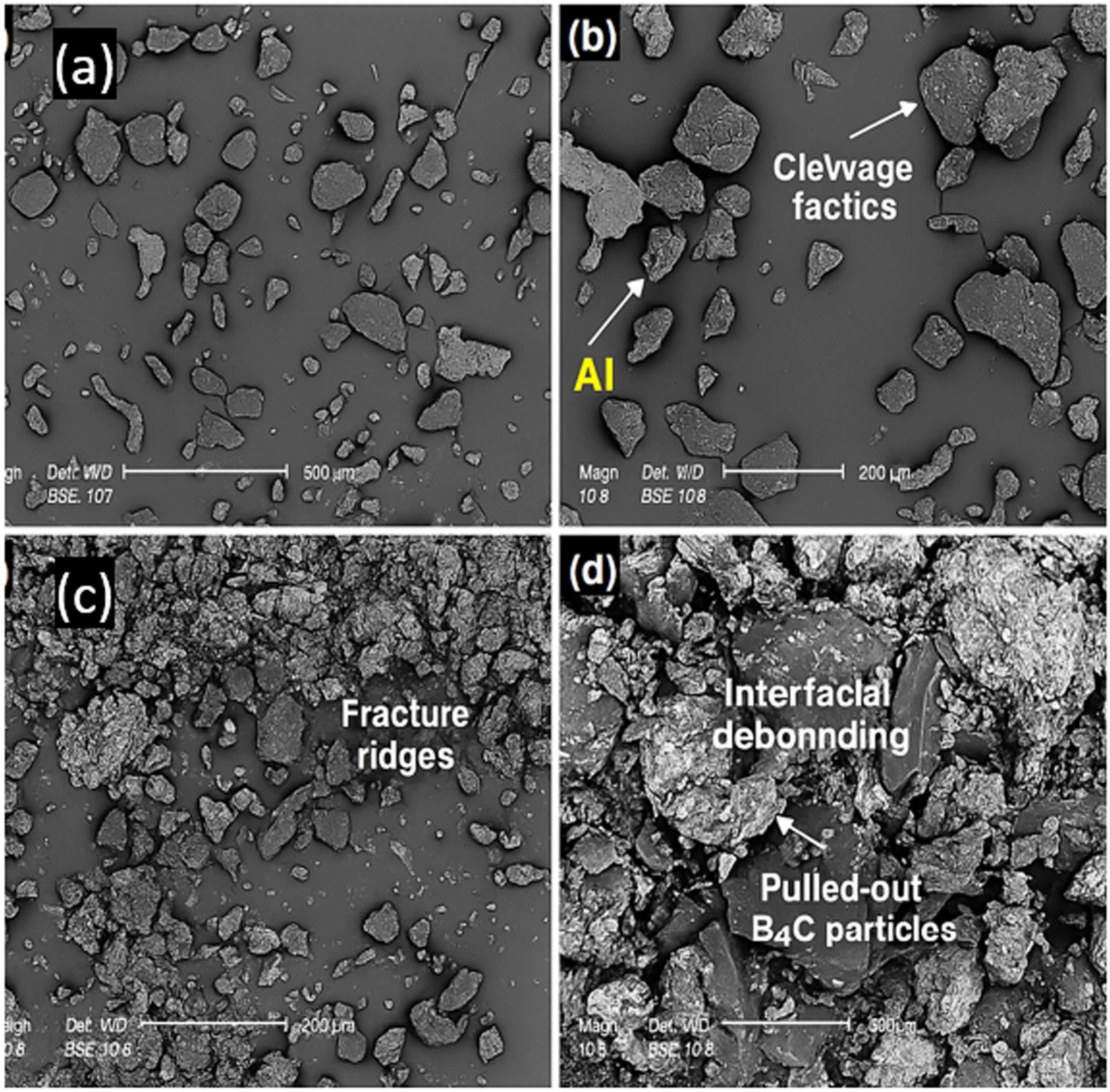

Figure 7. Fracture-surface SEM of Al–B_4C composites after tensile testing. (a) Overview of the fracture topology with dispersed particles (50×; 500 μm bar). (b) Medium-mag view highlighting matrix regions (Al) and angular B_4C fragments; cleavage facets appear on fractured particles (100×; 200 μm bar). (c) Region showing fracture ridges and debris fields consistent with microvoid coalescence (100×; 200 μm bar). (d) High-mag region showing interfacial debonding and pulled-out B_4C particles (200×; 100 μm bar), evidencing mixed ductile–brittle fracture where clustering occurs.

The faint TiC/Al–Ti reflections at near-LoD levels, together with residual K_2TiF_6 and localized Ti–F signals at interfaces, indicate incomplete flux consumption and localized Ti-mediated wetting, rather than bulk intermetallic strengthening. Transmission electron microscopy (TEM) was not performed in this study; definitive nanoscale interfacial identification (nm-scale TiC/Al–Ti) is deferred to future work.

3.4 Mechanical properties—hardness behavior of B_4C-Reinforced AA6061 Composites

Figure 10 shows the changes in both microhardness and macrohardness as B_4C content increases. A consistent upward trend was observed in the range of 4–12 wt.%. The Brinell hardness (BHN) of the unreinforced AA6061 matrix was ~35, rising to 83 BHN at 12 wt.% (~+137%). Similarly, the Vickers microhardness increased from 68 → 113 $HV_{0.5}$ (~+62%). This increase can be attributed to the mechanical rigidity of B_4C, effective load transfer, and

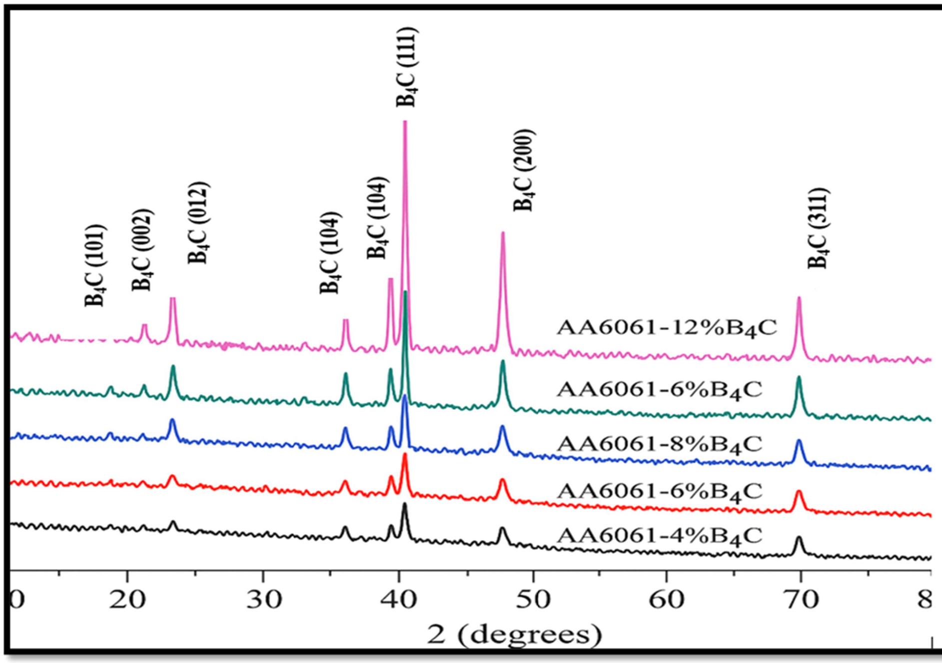

Figure 8. X-ray diffraction (XRD) patterns of AA6061-B_4C composites with different B_4C concentrations.

strong interfacial adhesion between the matrix and the reinforcement phase. The Vickers microhardness (HV) and Brinell macrohardness (BHN) show a strong linear relation based on means $(n = 3) \pm 1$ SD: $HV = 0.79 \times BHN + 46.3$ ($R^2 = 0.946$, $p < 0.01$). This agreement across 0–12 wt.% B_4C indicates that both indentation scales track the same matrix–particle load-transfer response. Small departures at ≥ 10 wt.% are consistent with localized strain gradients/porosity, in line with the σ_a and $\bar{\lambda}$ dispersion metrics. The low scatter in both series (SD $\lesssim$ 3%) supports measurement reproducibility and the reliability of the flux-assisted dispersion regime. Notably, there was no agglomeration-induced softening, even at the highest reinforcement loading, suggesting a uniform dispersion of particulates. This uniformity is likely supported using K_2TiF_6 as a fluxing and wetting agent. Similar findings have been documented in the literature, where the incorporation of fluxes like K_2TiF_6 improved wettability and minimized particle clustering in Al-based composites [31–35]. $HV = 10.3 \times BHN–12.5$.

SEM of the tensile fracture surfaces (Fig. Y) shows predominantly dimpled rupture with fracture ridges at ≤10 wt.% B_4C, while regions of higher local particle density exhibit cleavage facets on B_4C and particle–matrix debonding/pull-out at 12 wt.%. The rise in brittle features coincides with the dispersion transition (σ_a increases from ≤4.8% to 11.2% at 12 wt.% and $\bar{\lambda}$ reaches ~16 μm), explaining the modest UTS gain but reduced ductility at the highest loading. Together with XRD/EDS evidence of only trace TiC/Al–Ti near the LoD and localized Ti–F at interfaces, this supports Ti-mediated wetting with clustering-driven strain localization rather than bulk intermetallic strengthening.

The observed enhancement in hardness is driven by several microstructural strengthening mechanisms. First, Orowan strengthening is significant, as dislocation loops form around well-dispersed B_4C particles, increasing resistance to dislocation movement [36–38]. Second, dislocation pile-up at the reinforcement-matrix interfaces creates internal stress fields that hinder plastic deformation [39,40]. Lastly, the intrinsic hardness of B_4C (~30 GPa) directly enhances the composite's resistance to indentation [41,42]. These mechanisms align with established models of ceramic-particle reinforcement in metal matrix composites (MMCs) [3], where dispersion strengthening and interface-controlled mechanisms play a key role in hardness evolution. Collectively, these mechanisms result in a refined and mechanically resilient microstructure that resists both localized and distributed deformation. This is especially important for applications where hardness is directly related to wear resistance and dimensional stability under operational stresses, such as in brake components, valve seats, and other high-contact areas in automotive and aeronautical systems.

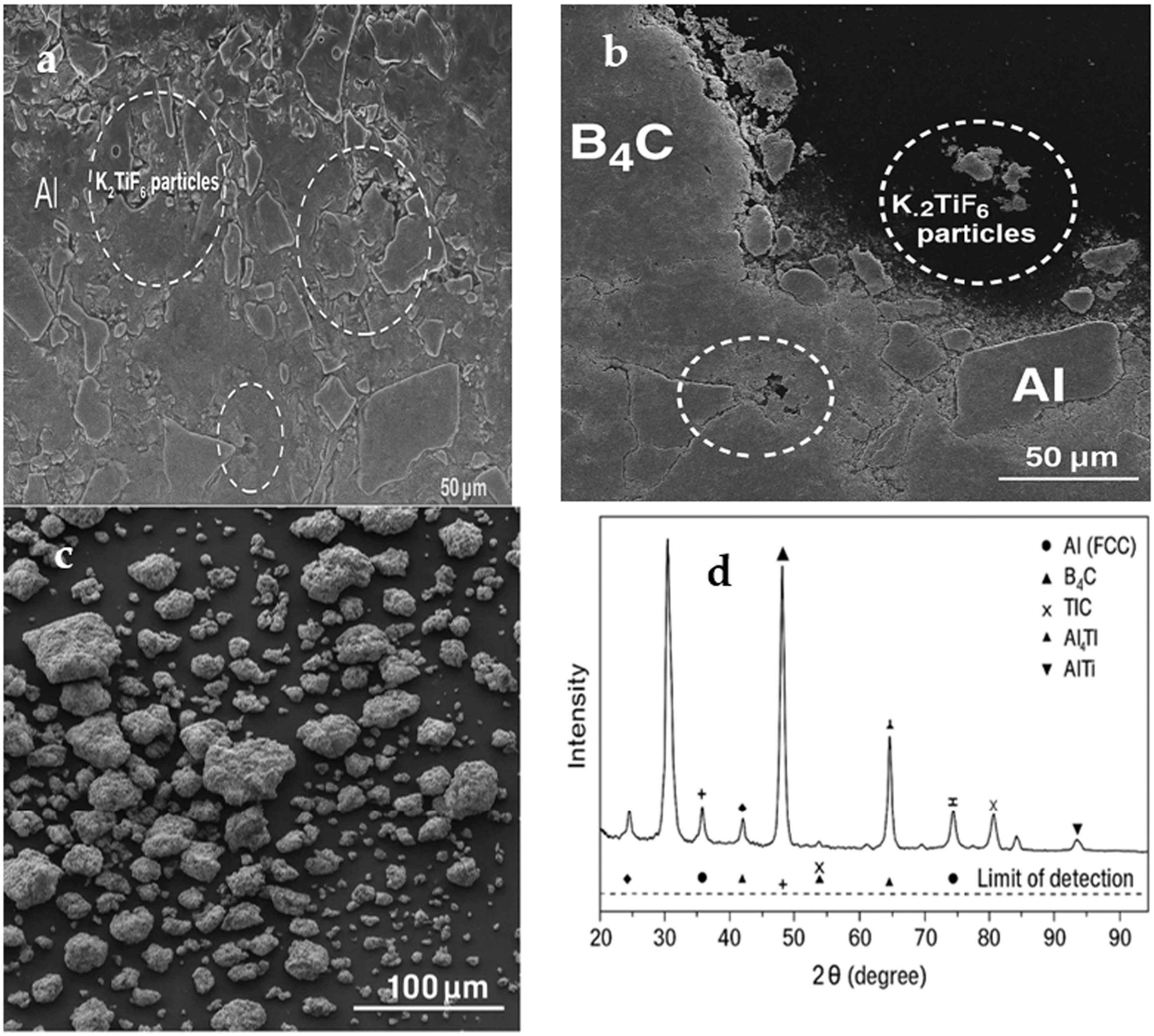

Figure 9. (a,b) SEM images of Al–B_4C microstructure showing residual K_2TiF_6 particles at/near the interface (dashed circles); scale = 50 µm. (c) Representative agglomerated precursor/residual flux morphology; scale = 100 µm. (d). XRD pattern (Cu Kα): strong Al (FCC) and B_4C peaks; TiC and Al–Ti (Al_3Ti/AlTi) reflections are present near the limit of detection, consistent with trace reaction products from K_2TiF_6-assisted casting rather than bulk phase formation.

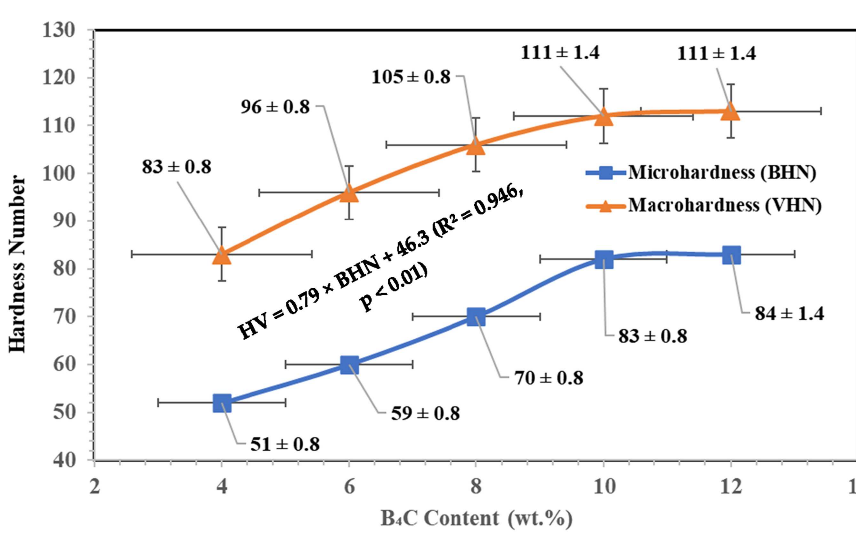

Figure 10. Effect of B_4C content on hardness, including standard deviation ($n = 3$).

3.5 Mechanical properties—tensile strength evolution with B_4C Reinforcement

As shown in Figure 11, the unreinforced control measured 142 ± 3.5 MPa, increasing to 215 ± 3.2 MPa at 12 wt.% B_4C, a + 51.4% gain (group means, $n = 3$). This enhancement highlights the synergy between the ductile matrix and the hard ceramic phase, driven by a combination of microstructural and interface strengthening mechanisms. First, the use of K_2TiF_6 as a fluxing agent significantly improves the wettability between the B_4C particles and the aluminum melt, ensuring uniform distribution and reducing interfacial defects. Previous studies [43,44], have indicated that this treatment enhances particle-matrix bonding, facilitating more efficient load transfer during tensile loading.

Second, grain refinement and boundary stabilization are critical to the observed strength increase. The uniformly distributed B_4C particles act as effective nucleation sites and pinning agents that obstruct grain boundary movement during solidification, resulting in a finer microstructure. According to the Hall–Petch relationship, this refinement leads to higher tensile strength [45–47]. Furthermore, Orowan strengthening enhances the alloy's resistance to plastic deformation [37,48]. The non-shearable nature of B_4C particulates compel dislocations to bow around them, increasing dislocation density and hindering movement, a mechanism that is particularly effective at the sub-micron scale [49,50]. This effect becomes more pronounced with higher reinforcement content, provided the particles are well dispersed and not agglomerated. Collectively, these mechanisms create a composite structure capable of withstanding higher tensile loads while maintaining ductility. The observed trend in strengthening is consistent with previous research on B_4C-reinforced Al-based composites, which have consistently reported moderate to significant UTS improvements based on processing methods, particle size, and volume fraction [41,51].

3.6 Reinforcement saturation and comparative performance of B_4C composites

The observed saturation in tensile strength beyond a specific B_4C content indicates diminishing returns, where the mechanical benefits of additional reinforcement are offset by microstructural irregularities, such as particle clustering, increased porosity, and stress concentration zones. These issues are well-documented in particulate-reinforced metal matrix composites (MMCs) and become especially pronounced when critical dispersion thresholds are exceeded [52,53].

Comparative analysis shows that B_4C-reinforced AA6061 composites demonstrate equal or superior ultimate tensile strength (UTS) compared to their SiC- and Al_2O_3-reinforced counterparts, even at lower reinforcement weight fractions. This advantage is particularly notable when employing flux-assisted casting

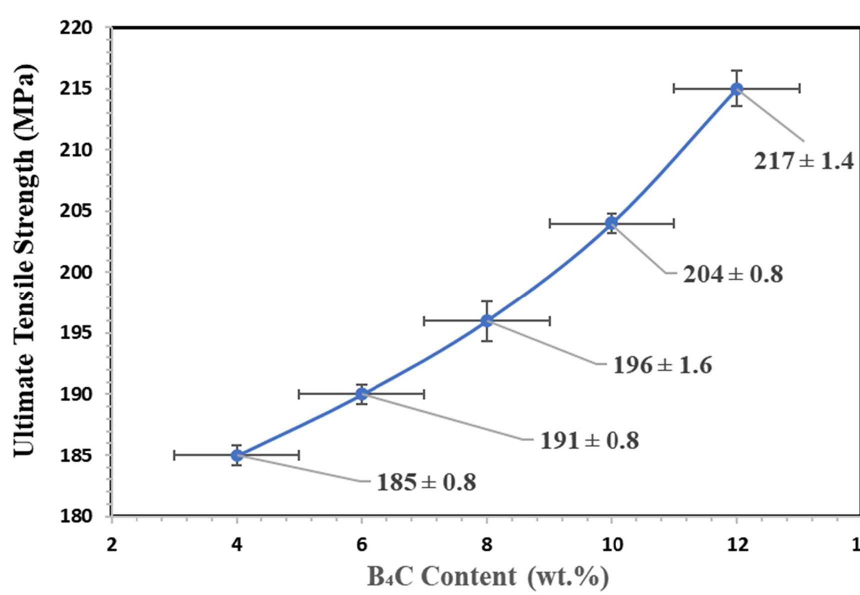

Figure 11. Effect of B_4C content on ultimate tensile strength (UTS), including standard deviation ($n = 3$).

techniques, such as those using K_2TiF_6, which promote effective particle wetting and uniform distribution [54,55]. The flux helps reduce particle agglomeration and improves interfacial bonding, facilitating a more efficient load transfer under tensile stress [56]. These findings are consistent with those reported in [57], which indicated that intermediate B_4C loadings, rather than extreme concentrations, lead to the most favorable mechanical outcomes. Their study emphasized that uniform dispersion and optimal particle-matrix compatibility are more crucial than the volume of reinforcement in determining composite strength. Additionally, other researchers have noted that excessive reinforcement beyond a critical threshold often introduces structural defects,compromising mechanical reliability [58]. The mechanical property trends by weight percent B_4C are summarized in Table 2. All mechanical property values are reported as group means ± standard deviation (SD) from three independent specimens ($n = 3$). Error bars in corresponding figures represent ± 1 SD.

Table 3 summarizes the distinct processability benefits of B_4C-based systems, especially when advanced casting protocols are used. These benefits include reduced tool wear, improved fluidity, and enhanced composite integrity, all of which are essential for scaling up to industrial applications in automotive and aeronautical manufacturing [59].

3.7 Predictive modeling and theoretical correlation

The experimental ultimate tensile strength (UTS) values closely aligned with predictions from the Rule of Mixtures (ROM) within the 4–8 wt.% B_4C range but diverged significantly beyond 10 wt.%. This trend highlights the inherent limitations of linear predictive models in capturing the complexity of real composite systems, particularly as the content of reinforcement increases and microstructural irregularities, such as particle clustering, porosity, and interfacial debonding, begin to dominate the mechanical response [60,61]. The ROM offers a first-order estimate of composite strength based on the volume-weighted contributions of the matrix and reinforcement phases, as outlined in Equation 6:

$$\sigma_c = V_m \sigma_m + V_r \sigma_r \tag{6}$$

Table 2. Comparison of mechanical and physical properties of AA6061–B_4C composites by B_4C wt.% (mean ± SD, $n = 3$).

B_4C (wt %)	BHN	$HV_{0.5}$	UTS (MPa)	% Elongation	Density (g cm^{-3})	Porosity (%)	Dispersion quality	Remarks
0	35 ± 1.1	68 ± 2.0	142 ± 3.5	12.4 ± 0.3	2.69 ± 0.01	1.5 ± 0.1	Uniform (baseline)	Unreinforced alloy
4	52 ± 1.3	83 ± 2.1	185 ± 4.0	11.2 ± 0.2	2.68 ± 0.01	2.0 ± 0.1	Uniform	Marked UTS gain from B_4C initiation
6	60 ± 1.4	96 ± 2.0	190 ± 3.8	10.9 ± 0.3	2.67 ± 0.01	1.6 ± 0.2	Excellent	Strengthening via refined grain structure
8	70 ± 1.5	106 ± 2.3	196 ± 3.6	10.3 ± 0.2	2.66 ± 0.01	2.5 ± 0.2	Very Good	Approaching optimal UTS performance
10	82 ± 1.6	113 ± 2.5	204 ± 3.4	9.8 ± 0.2	2.65 ± 0.01	3.0 ± 0.3	Optimal	Peak hardness and microstructural balance
12	83 ± 1.5	110 ± 2.3	215 ± 3.2	9.3 ± 0.3	2.64 ± 0.01	3.5 ± 0.3	Agglomerated	UTS peak reached; dispersion less ideal, but not detrimental

Footnote: All samples were fabricated under identical conditions (melt ≈ 750 °C, stir ≈ 600 rpm, 10 min, steel mold ≈ 250 °C) using K_2TiF_6 = 1 wt % as the fluxing agent. Hardness values correspond to Vickers $HV_{0.5}$ (4.903 *N* load) and Brinell (10 mm ball, 500 kg load).

Table 3. Comparative performance of B_4C with other reinforcements in AA6061 matrix.

Reinforcement	Optimal wt.%	Microhardness (HV)	UTS (MPa)	Remarks
B_4C	12	35–60	215	Strength and hardness increased by up to 12 wt.% due to excellent dispersion and bonding facilitated by K_2TiF_6. No softening from agglomeration.
SiC	10–15	100–110	185–200	Well-dispersed but prone to agglomeration >12 wt.%. Exhibits good overall mechanical properties.
Al_2O_3	10–15	95–105	170–185	High hardness with moderate UTS due to weaker matrix-particle interactions.
Fly Ash	10–15	80–95	160–175	Economical; with variable bonding and dispersion resulting in lower consistency.
Graphite	4–6	70–80	145–160	Improves wear resistance through solid lubrication but reduces tensile strength.

where σ_c represents the predicted ultimate tensile strength of the composite, V_m and V_r denote the volume fractions of the matrix and reinforcement, respectively, and σ_m and σ_r are their corresponding tensile strengths. To convert weight% to volume%, the densities of the matrix and reinforcement are used. The formula for the volume fraction of reinforcement is provided in Equation 7:

$$V_r = \frac{W_r/\rho_r}{(W_r/\rho_r) + (W_m/\rho_m)} \tag{7}$$

where V_r represents the volume fraction of reinforcement; W_r denotes the weight fraction of reinforcement; W_m is the weight fraction of the matrix, calculated as $W_m = 100 - W_r$; 0114_r signifies the density of the reinforcement ($B_4C \approx 2.52$ g.cm^{-3}); 0114_m indicates the density of the matrix (AA6061 ≈2.70 g.cm^{-3}). In this study, the matrix tensile strength was taken to be 142 MPa for unreinforced AA6061, while the reinforcement strength was assumed to be 450 MPa. This estimate is supported by literature and falls within the commonly cited range of 400–500 MPa for sintered B_4C ceramics [62–64]. This value has also been used in previous modeling efforts to approximate the strengthening effect of ceramic particulates in aluminum-based composites.

As shown in Figure 12, the predictions from the Rule of Mixtures (ROM) closely aligned with experimental ultimate tensile strength (UTS) values at lower reinforcement levels, indicating effective stress transfer and minimal microstructural disruption. However, at 10 wt.% and particularly at 12 wt.%, the experimental UTS values surpassed the ROM estimates. This suggests that additional mechanisms, such as dislocation pile-up, Orowan strengthening, and particle–matrix interlocking, were in play. Concurrently, localized heterogeneities, including increased porosity and agglomeration, likely began to introduce non-uniform strain fields that linear ROM models cannot account for. To better represent these nonlinearities, prior studies have employed semi-empirical models, such as the Halpin-Tsai equation, to incorporate the effects of reinforcement geometry and distribution. Nevertheless, these models still assume idealized dispersion and bonding, which limits their predictive accuracy in systems with significant interfacial degradation [65,66]. To address these limitations, future work will utilize multiscale modeling frameworks, including representative volume element (RVE)-based finite element simulations, to explicitly account for particle–matrix interactions, void distributions, and local stress concentrations.

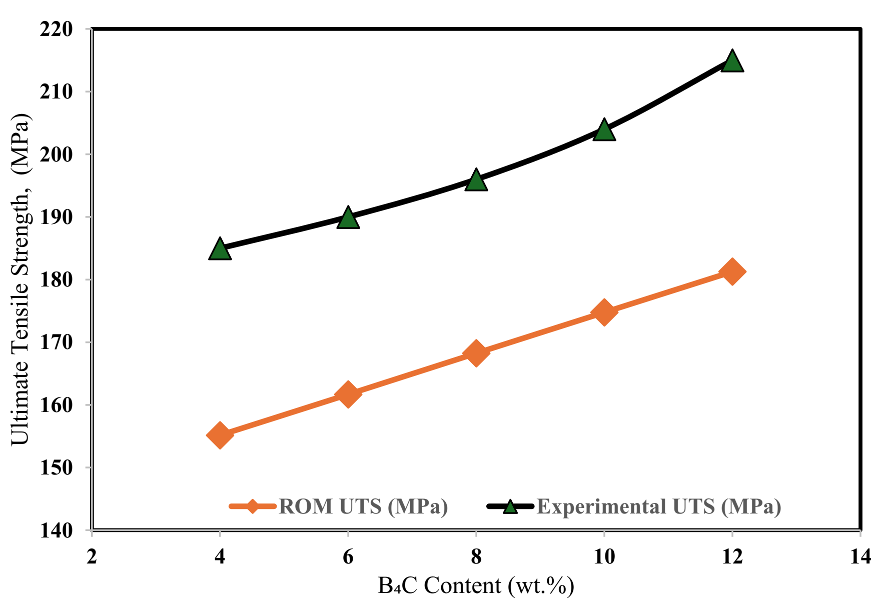

Figure 12. Comparison of the ultimate tensile strength (UTS) of AA6061-B_4C composites: experimental results vs. rule of mixtures predictions (values are mean ± SD, $n = 3$).

3.8 Structure-property relationships

A clear and quantifiable relationship was identified between processing conditions, microstructural evolution, and the resulting mechanical performance. The use of flux-assisted stir casting with K_2TiF_6 significantly improved particle–matrix interactions by enhancing wettability, minimizing interfacial porosity, and promoting uniform dispersion of B_4C across most reinforcement levels [67]. For composite materials containing up to 10 wt.% B_4C, there were consistent increases in both microhardness and tensile strength. These improvements were attributed to enhanced particle bonding, reduced defect concentration, and refined grain structure. Notably, the 10 wt.% sample exhibited the most balanced profile, featuring optimal dispersion, moderate porosity (3.0%), the highest measured microhardness (113 $HV_{0.5}$), and a robust ultimate tensile strength (UTS) of 204 MPa.

Interestingly, at 12 wt.% B_4C, performance did not decline as expected. Instead, both hardness and UTS reached their peak values of 113 $HV_{0.5}$ and 215 MPa, respectively, despite a slight increase in porosity (3.5%) and observable signs of particle agglomeration. This indicates that while the quality of dispersion may have decreased, the higher volume fraction of reinforcing B_4C continued to positively influence load-bearing capacity. These findings support previous reports [68,69] suggesting that moderate clustering may not always be detrimental and can, in some cases, enhance uniaxial strength in ceramic-reinforced metal matrix systems. However, this trend may not apply to fatigue, impact, or wear properties, where microstructural uniformity and defect suppression are more critical. Consequently, the 12 wt.% composition represents a high-strength but potentially brittle configuration, warranting further investigation.

3.9 Summary of microstructural and mechanical findings

The results indicate a strong progression in composite behavior with increasing B_4C content. From 0 to 10 wt%, mechanical properties consistently improved due to effective stress transfer, grain refinement, and enhanced particle–matrix bonding. At 10 wt%, the composite reached optimal microstructural harmony and mechanical synergy, characterized by excellent dispersion and a favorable balance between porosity and reinforcement load. At 12 wt%, the ultimate tensile strength (UTS) peaked at 215 MPa, and hardness saw a slight increase to 113 $HV_{0.5}$. However, this was accompanied by a decline in dispersion quality and an increase in porosity. This suggests that mechanical maxima can still be achieved despite early-stage agglomeration, if interfacial integrity remains largely intact. These trends are summarized in Table 4, which illustrates the intricate relationship between dispersion quality, porosity, and mechanical response throughout the reinforcement spectrum. These results reinforce the principles of composite design, highlighting the importance of balanced reinforcement, where enhancements in mechanical properties are carefully considered alongside the risk of potential microstructural instability [70–72].

3.10 Practical implications, outlook, and limitations of the study

These findings underscore the viability of B_4C as a reinforcement for engineering-grade aluminum composites. When processed with appropriate fluxing and stirring protocols, B_4C-reinforced AA6061 can achieve high hardness and strength at relatively low weight fractions, making it an excellent candidate for applications such as automotive brake rotors, aerospace panels, and wear-resistant components. Equally important is the role of process optimization: material choice alone is insufficient without precise control of reinforcement distribution and interfacial quality. Future work should explore tribological and fatigue

Table 4. Summary of key microstructural and mechanical findings (values are mean ± SD, $n = 3$).

B_4C (wt.%)	Dispersion quality	Porosity (%)	($HV_{0.5}$)	UTS (MPa)	Key observations
0	Uniform (baseline)	1.5	68	142	Unreinforced matrix
4	Uniform	2.0	83	185	Homogeneous particle introduction
6	Excellent	1.6	96	190	Improved bonding and refinement
8	Very Good	2.5	106	196	Near-optimal performance
10	Optimal	3.0	113	204	Peak strength and hardness
12	Agglomerated	3.5	110	215	UTS peaks despite slight clustering

properties, as well as life cycle assessments to evaluate the broader economic and environmental impacts of scaling these composites for real-world applications. Integrated experimental and simulation-based approaches will be central to this transition, ensuring the composites not only meet structural performance criteria but also align with sustainability and cost-efficiency goals in high-tech sectors.

While the study demonstrates significant enhancements in the mechanical performance of AA6061-B_4C composites using flux-assisted stir casting, certain limitations must be acknowledged. First, the mechanical testing focused primarily on static properties (hardness and tensile strength); dynamic behaviors such as fatigue life, impact resistance, and creep deformation remain unexplored. Second, the reinforcement particle size and morphology were not varied systematically, which may influence dispersion behavior and interfacial bonding. Third, the potential chemical reactivity of K_2TiF_6 with other alloying elements or trace impurities in industrial-grade melts was not thoroughly investigated. Additionally, while the porosity measurements are indicative, they could benefit from more advanced imaging or X-ray tomography to quantify internal voids with greater resolution. These limitations provide valuable directions for future research and process refinement.

4 Conclusion and future direction

A scalable, industry-compatible flux-assisted stir casting route was demonstrated for AA6061-B_4C. A low-dose K_2TiF_6 window (0.5–1.0 wt.%) disrupted oxide films, improved wettability, and enabled near-uniform dispersion to 10 wt.% B_4C. Under the finalized stirring regime (600 rpm, 10 min), entrainment efficiency and porosity control were balanced, enabling reproducible structure–property outcomes across 4–12 wt.% B_4C. Microstructural evidence (SEM/EDS/XRD) confirmed clean particle-matrix interfaces and refined as-cast grains. Correspondingly, microhardness ($HV_{0.5}$) increased from 68 to 113 (+60%; group means, $n = 3$), and UTS reached 215 MPa, a +51.4% gain relative to the unreinforced control (142 MPa; group means, $n = 3$). While dispersion quality is optimal around 10 wt.%, peak UTS occurs at 12 wt.%, where incipient clustering and modest porosity (3.5%) begin to offset further strengthening gains. These results emphasize that process engineering (flux dose + hydrodynamics), as much as reinforcement level, governs final properties in cast AMCs. Practically, the process offers a cost-effective, energy-lean, high-throughput alternative to multi-step routes, with immediate relevance to automotive, aerospace, defense, and structural applications demanding lightweight, wear-resistant, high-strength components.

Future work will (i) quantify image-based porosity and fracture initiation sites to tighten the mechanism–property link, (ii) extend to tribology and fatigue to validate service performance [8], and (iii) explore hybrid reinforcements and process windows (impeller geometry/speed, dwell) to widen the operating envelope while maintaining low defect content.

In summary, this work advances a flux-modified casting paradigm for engineering aluminum matrix composites that are not only mechanically robust but also economically and environmentally viable. By bridging fundamental processing science with scalable manufacturing, the proposed approach offers a viable pathway toward next-generation composite materials capable of meeting the evolving demands of high-performance, low-weight engineering systems.

4.1 Impact statement

This study presents a flux-engineered stir casting method that employs K_2TiF_6 to enhance the dispersion, wettability, and interfacial bonding of B_4C particles in AA6061 composites. This method is both scalable and cost-effective, leading to increases of ~60% in microhardness (68 → 113 $HV_{0.5}$) and ~51% in UTS (142 → 215 MPa), reported as group means ($n = 3$). Structural uniformity and improved material properties are validated through SEM, EDS, and XRD analyzes, with additional insights gained from ROM analysis. This research advances the manufacturing of sustainable, high-performance materials and is particularly relevant for the aerospace, automotive, building, construction, and defense sectors, which are in search of lightweight, durable, and energy-efficient solutions. It also supports the goals of the circular economy by promoting the principles of reuse, reduction, recovery, and recycling (4R's).

Acknowledgements

The authors wish to express their gratitude to Kampala International University, Uganda; Kabale University, Uganda; and King Faisal University, Saudi Arabia, for offering a supportive environment that greatly facilitated the successful conduct of this study.

Author contributions

None.

Disclosure statement

The authors affirm that the content of this manuscript is original and that they possess full legal rights to the intellectual property contained within. They also grant permission for this article to be published.

Funding

This work was supported by the Deanship of Scientific Research, Vice Presidency for Graduate Studies and Scientific Research, King Faisal University, Saudi Arabia [Grant No. KFU254082].

Data availability statement

The analyzed data are included within the article.

References

[1] Chen B, Sun H, Ye Y, et al. Research status and development trends of joining technologies for ceramic matrix composites. Materials. 2025;18:871. doi: 10.3390/MA18040871
[2] Ammendola M, Kedir N, Ghoshal A, et al. Mechanical properties of ultra-high temperature ceramic matrix composites (UHTCMCs): a review. Ceram Int. 2025;51:29845–29876. doi: 10.1016/J.CERAMINT.2025.04.293
[3] Shrivastava S, Rajak D, Joshi T, et al. Ceramic matrix composites: classifications, manufacturing, properties, and applications. Ceramics. 2024;7:652–679.
[4] Barah O, Onyelowe K, Olotu E, et al. Aluminium 6061 and hybridized agro-marine waste particulate composite: review. IDOSR JOURNAL OF SCIENCE AND TECHNOLOGY. 2023;9:83–99. doi: 10.59298/IDOSR/JST/03.1.12007
[5] Barah O, Dennison M, Nnamchi S, et al. Physical, chemical, and mineralogical properties of agromarine waste ash. DiMat. 2025;5(1):1–15. doi: 10.1007/S43939-025-00244-4
[6] Soundararajan R, Sathishkumar A, Sivasankaran S, et al. Evaluation of microstructures, mechanical and dry-sliding wear performance of A356-(Fly Ash/SiCp) hybrid composites. Int J Metalcast. 2022;16:2079–2096. doi: 10.1007/S40962-021-00731-3/METRICS
[7] Kaviyarasan K, Soundararajan R, Raj A, et al. Assessment of mechanical and tribological characteristics of A356 reinforced with x wt% CaB6 composites. JIEID. 2021;103(1):75–84. doi: 10.1007/S40033-021-00303-Z
[8] Soundararajan R, Sathishkumar A, Feroz Ali L, et al. Exploration of various forging route performance of cast A356 alloy reinforced with Fly Ash and MWCNT hybrid composites. JIEID. 2022;104(1):259–268. doi: 10.1007/S40033-022-00401-6
[9] Kuliiev R. Mechanical Properties of Boron Carbide (B4C). Electronic Theses and Dissertations, 2020-2023. 2020
[10] Kar A, Sharma A, Kumar S. A critical review on recent advancements in aluminium-based metal matrix composites. Crystals. 2024;14:412. doi: 10.3390/CRYST14050412
[11] Kumar A, Singh V, Singh R, et al. A review of aluminum metal matrix composites: fabrication route, reinforcements, microstructural, mechanical, and corrosion properties. J Mater Sci. 2024;59(7):2644–2711. doi: 10.1007/S10853-024-09398-7
[12] Rong X, Zhao D, He C, et al. Review: recent progress in aluminum matrix composites reinforced by in situ oxide ceramics. J Mater Sci. 2023;59(22):9657–9684. doi: 10.1007/S10853-023-09120-Z
[13] Wang Z, Zheng Z, Fu M. Aluminum matrix composites: structural design and microstructure evolution in the deformation process. Journal of Materials Research and Technology. 2024;30:3724–3754. doi: 10.1016/J.JMRT.2024.03.237
[14] Hussein H, Wang Z, Alani W, et al. A novel experimental design for free energy from the heat-gaining panel using multi-thermoelectric generators (TEGs) panel. Case Studies in Thermal Engineering. 2023;50:103431. doi: 10.1016/J.CSITE.2023.103431
[15] Kaviyarasan K, Soundararajan R, Roger R, et al. Assessing the tribological behaviour of stir casted AA 6063 with xwt% ZrSiO4 and 6wt% TiB2 hybrid composites. JIEID. 2022;103(1):85–94. doi: 10.1007/S40033-021-00306-W

[16] Thillikkan S, Kumar N, Francis LKM, et al. Stir Casting Synthesis and Evaluation of SiC Nanoparticle-Reinforced AZ31 Magnesium Alloy Nanocomposites SAE Technical Papers. 2025. doi: 10.4271/2025-01-5013
[17] Mazaheri Y, Emadi R, Meratian M, et al. An experimental investigation of effects of fluxes (Na3AlF6 and K2TiF6), element alloys (Mg), and composite powders ((Al + TiC)CP and (Al + B4C)CP) on distribution of particles and phases in Al-B4C and Al-TiC composites. Metall Mater Trans B. 2017;48:1279–1291. doi: 10.1007/S11663-016-0900-X/METRICS
[18] Randhawa K. A state-of-the-art review on advanced ceramic materials: fabrication, characteristics, applications, and wettability. Pigment and Resin Technology. 2023;53:768–785. doi: 10.1108/PRT-12-2022-0144/FULL/XML
[19] Wang Z, Tao S, Deng J, et al. Significant improvement in the dehydriding properties of perovskite hydrides, NaMgH3, by doping with K2TiF6. Int J Hydrogen Energy. 2017;42:8554–8559. doi: 10.1016/J.IJHYDENE.2016.12.078
[20] Novita M, Ogasawara K. Comparative study of multiplet structures of Mn 4+ in K 2SiF 6, K 2GeF 6, and K 2TiF 6 based on first-principles configuration-interaction calculations. Jpn J Appl Phys. 2012;51:022604. doi: 10.1143/JJAP.51.022604/XML
[21] Juhasz K, Baumli P, Kaptay G. Fabrication of carbon fibre reinforced, aluminium matrix composite by potassium iodide (KI) – potassium hexafluoro-titanate (K2TiF6) fluxErzeugung kohlenstofffaserverstärkter Aluminiumverbunde mit Potassium Iodid – Potassium Hexafluor-Titanat (K2TiF6) als Schmelzmittel. Materwiss Werksttech. 2012;43:310–314. doi: 10.1002/MAWE.201200946
[22] Tambol S, Pandey A, Bongale AA, et al. Effect of machining of aluminium alloys with emphasis on aluminium 6061 alloy – a review. IOP Conf Ser Mater Sci Eng. 2021;1107:012157. doi: 10.1088/1757-899X/1107/1/012157
[23] Pandey U, Acherjee B, Paul G, et al. A novel integrated stir–ultrasonic–squeeze casting route for fabricating AA6061-based metal matrix hybrid nanocomposites with enhanced tribomechanical properties. J Micromech Microeng. 2025;35:095017. doi: 10.1088/1361-6439/AE08C2
[24] Pandey U, Ghose J, Acherjee B, et al. Mechanical and tribological performance of AA6061 hybrid nanocomposites produced by stir-ultrasonic-squeeze casting method. J Mater Eng Perform. 2025;2025:1–15. doi: 10.1007/S11665-025-12169-3
[25] Kumar C, Sarkar S, Mukhopadhyay G, et al. Systematic study of the effect of K2TiF6 flux content on the microstructure and mechanical properties of Al–B4C composites. Mater Sci Eng A. 2023;871:144913. doi: 10.1016/J.MSEA.2023.144913
[26] Kumar C, Sen I, Roy S. Synergistic effect of ex situ and in situ reinforcements on the dry reciprocating wear behavior of AA6061-B4C composite fabricated using varying K2TiF6 flux content. J Mater Eng Perform. 2024;34:1–21. doi: 10.1007/S11665-024-10106-4/METRICS
[27] Cai Y, Khan M, Yao W, et al. Study on the microstructure, mechanical and corrosion behaviors of 2A12 Al matrix composites containing B4C and 50% K2TiF6 flux. Materials Science and Technology (United Kingdom). 2024. doi: 10.1177/02670836241281125
[28] Gao K, Zhang Y, Yi J, et al. Overview of surface modification techniques for titanium alloys in modern material science: a comprehensive analysis. Coatings. 2024;14:148. doi: 10.3390/COATINGS14010148
[29] Kamanna B, Kivade S, Nagamadhu M. Effect of zirconium silicate reinforcement on aluminum 7075; mechanical properties, thermomechanical analysis and vibrational behavior. Eng. 2025;6:23. doi: 10.3390/ENG6020023
[30] Gudipudi S, Nagamuthu S, Subbian K, et al. Enhanced mechanical properties of AA6061-B4C composites developed by a novel ultra-sonic assisted stir casting. Engineering Science and Technology, an International Journal. 2020;23:1233–1243. doi: 10.1016/j.jestch.2020.01.010
[31] Sijo M, Jayadevan K. Analysis of stir cast aluminium silicon carbide metal matrix composite: a comprehensive review. Procedia Technology. 2016;24:379–385. doi: 10.1016/J.PROTCY.2016.05.052
[32] Gopalakrishnan S, Murugan N. Production and wear characterisation of AA 6061 matrix titanium carbide particulate reinforced composite by enhanced stir casting method. Compos B Eng. 2012;43:302–308. doi: 10.1016/J.COMPOSITESB.2011.08.049
[33] Sharma S, Singh J, Gupta M, et al. Investigation on mechanical, tribological and microstructural properties of Al–Mg–Si–T6/SiC/muscovite-hybrid metal-matrix composites for high strength applications. Journal of Materials Research and Technology. 2021;12:1564–1581. doi: 10.1016/J.JMRT.2021.03.095
[34] Samal P, Vundavilli P, Meher A, et al. Recent progress in aluminum metal matrix composites: a review on processing, mechanical and wear properties. J Manuf Process. 2020;59:131–152. doi: 10.1016/J.JMAPRO.2020.09.010
[35] Sun J, Ye D, Zou J, et al. A review on additive manufacturing of ceramic matrix composites. J Mater Sci Technol. 2023;138:1–16. doi: 10.1016/J.JMST.2022.06.039
[36] Barnett M, Wang H, Guo T. An orowan precipitate strengthening equation for mechanical twinning in Mg. Int J Plast. 2019;112:108–122. doi: 10.1016/J.IJPLAS.2018.08.010
[37] Peng S, Wang Z, Li J, et al. Beyond orowan hardening: mapping the four distinct mechanisms associated with dislocation-precipitate interaction. Int J Plast. 2023;169:103710. doi: 10.1016/J.IJPLAS.2023.103710
[38] Zhang Y, Sills R. Strengthening via orowan looping of misfitting plate-like precipitates. J Mech Phys Solids. 2023;173:105234. doi: 10.1016/J.JMPS.2023.105234
[39] Guan C, Chen G, Kai X, et al. Transformation of dislocation strengthening mechanisms induced by graphene nanoplates and ZrB2 nanoparticle in nanolaminated Al matrix composites. Mater Charact. 2023;199:112773. doi: 10.1016/J.MATCHAR.2023.112773

[40] Peng Y, Ji R, Phan T, et al. An atomistic-to-microscale computational analysis of the dislocation pileup-induced local stresses near an interface in plastically deformed two-phase materials. Acta Mater. 2022;226:117663. doi: 10.1016/J.ACTAMAT.2022.117663
[41] Dai J, Singh J, Yamamoto N. Fracture toughness measurement for B4C composites with hierarchical microstructures: comparison of micro-indentation and four-point bending methods. J Test Eval. 2024;52:2967–2981. doi: 10.1520/JTE20240089
[42] Wang H, Zeng Y, Zhu T, et al. Exceptional strength-toughness-hardness integrated B4C ceramics with synergistic reinforcement of nano-BN and in-situ ceramic phases. Compos B Eng. 2025;288:111921. doi: 10.1016/J.COMPOSITESB.2024.111921
[43] Kumar A, Singh R, Chaudhary R. Recent progress in production of metal matrix composites by stir casting process: an overview. Mater Today Proc. 2020;21:1453–1457. doi: 10.1016/J.MATPR.2019.10.079
[44] Nirala A, Soren S, Kumar N, et al. A comprehensive review on mechanical properties of Al-B4C stir casting fabricated composite. Mater Today Proc. 2020;21:1432–1435. doi: 10.1016/J.MATPR.2019.09.172
[45] P B, M A. Effect of B4C and graphene on the microstructural and mechanical properties of Al6061 matrix composites. Journal of Materials Research and Technology. 2024;31:496–505. doi: 10.1016/J.JMRT.2024.06.098
[46] Ren R, Fan J, Wang B, et al. Hall-Petch relationship and deformation mechanism of pure Mg at room temperature. J Alloys Compd. 2022;920:165924. doi: 10.1016/J.JALLCOM.2022.165924
[47] Ondicho I, Alunda B, Park N. Effect of Fe on the hall-petch relationship of (CoCrMnNi)100-x Fex medium-and high-entropy alloys. Intermetallics (Barking). 2021;136:107239. doi: 10.1016/J.INTERMET.2021.107239
[48] Barah O, Onyelowe K, Olotu E, et al. Aluminium 6061 and Hybridized Agro-Marine Waste Particulate Composite: Review. n.d. doi: 10.59298/IDOSR/JST/03.1.12007
[49] Balakrishnan M, Dinaharan I, Palanivel R, et al. Influence of friction stir processing on microstructure and tensile behavior of AA6061/Al3Zr cast aluminum matrix composites. J Manuf Process. 2019;38:148–157. doi: 10.1016/J.JMAPRO.2018.12.039
[50] James J, Annamalai A, Muthuchamy A, et al. Effect of wettability and uniform distribution of reinforcement particle on mechanical property (Tensile) in aluminum metal matrix composite—a review. Nanomaterials. 2021;11:2230. doi: 10.3390/nano11092230
[51] Barah O, Onyelowe K, Nnamchi S, et al. Microstructure and toughness characterization of AA6061 hybrid composite reinforced with eucalyptus ash, periwinkle shell, and plantain fiber. Discover Applied Sciences. 2025;7:1–26. doi: 10.1007/S42452-025-06532-1/METRICS
[52] Dinaharan I, Balakrishnan M, David Raja Selvam J, et al. Microstructural characterization and tensile behavior of friction stir processed AA6061/Al2Cu cast aluminum matrix composites. J Alloys Compd. 2019;781:270–279. doi: 10.1016/J.JALLCOM.2018.12.091
[53] Bhoi N, Singh H, Pratap S. Developments in the aluminum metal matrix composites reinforced by micro/nano particles – a review. J Compos Mater. 2020;54:813–833. doi: 10.1177/0021998319865307
[54] Gutema E, Bazhin V, Fedorov S. Wettability enhancement of aluminum metal matrix composite reinforced with magnesium coated silicon carbide particles. IOP Conf Ser Mater Sci Eng. 2019;560:012179. doi: 10.1088/1757-899X/560/1/012179
[55] Malaki M, Tehrani A, Niroumand B, et al. Wettability in metal matrix composites. Metals. 2021;11:1034. doi: 10.3390/MET11071034
[56] Ranjitha P, Bavan D, Ajaykumar B, et al. Investigation of mechanical properties of Al6061–SiC–B4C composites produced by using stir casting method. JIEID. 2024;106:339–351. doi: 10.1007/S40033-024-00649-0/METRICS
[57] Wang Y, Guo Y, Zhang Q. Study on tribological properties and process optimization of Al2O3-xTiO2 composite coatings prepared by plasma spraying. Mater Today Commun. 2025;44:112182. doi: 10.1016/J.MTCOMM.2025.112182
[58] Xu Y, Zhang Y, Wang G, et al. Examining the mechanical properties of B4C/SiC hybrid reinforced 7075Al matrix composites using fast hot pressure sintering technique. Mater Today Commun. 2025;42:111293. doi: 10.1016/J.MTCOMM.2024.111293
[59] Ni S, Yan J, Wei T, et al. Microstructure and tribological performances of Cr3C2- and B4C-added CoCrFeNiMo HEA coatings prepared by laser cladding. Surf Coat Technol. 2025;511:132279. doi: 10.1016/J.SURFCOAT.2025.132279
[60] Surappa M. Aluminium matrix composites: challenges and opportunities. Sadhana - Academy Proceedings in Engineering Sciences. 2003;28:319–334. doi: 10.1007/BF02717141
[61] Zhou M, Ren L, Fan L, et al. Progress in research on hybrid metal matrix composites. J Alloys Compd. 2020;838:155274. doi: 10.1016/J.JALLCOM.2020.155274
[62] Domnich V, Reynaud S, Haber R, et al. Boron carbide: structure, properties, and stability under stress. J Am Ceram Soc. 2011;94:3605–3628. doi: 10.1111/J.1551-2916.2011.04865
[63] Balaraj V, Kori N, Nagaral M, et al. Microstructural evolution and mechanical characterization of micro Al2O3 particles reinforced Al6061 alloy metal composites. Mater Today Proc. 2021;47:5959–5965. doi: 10.1016/J.MATPR.2021.04.500
[64] Abiodun Balogun O, Adewale Akinwande A, Adesoji Adediran A, et al. Microstructure and particle size effects on selected mechanical properties of waste glass-reinforced aluminium matrix composites. Mater Today Proc. 2022;62:4589–4598. doi: 10.1016/J.MATPR.2022.05.330

[65] Huang D, Wang W, Tang X, et al. A novel semi-empirical analytical method for stiffness prediction of unidirectional discontinuous-fiber composites. Compos Sci Technol. 2025;262:111087. doi: 10.1016/J.COMPSCITECH.2025.111087
[66] Horstemeyer M. Multiscale modeling: a review. Practical Aspects of Computational Chemistry: Methods, Concepts and Applications. 2009;87–135. doi: 10.1007/978-90-481-2687-3_4
[67] Wu Q, Xu W, Zhang L. Microstructure-based modelling of fracture of particulate reinforced metal matrix composites. Compos B Eng. 2019;163:384–392. doi: 10.1016/J.COMPOSITESB.2018.12.099
[68] Aynalem G. Processing methods and mechanical properties of aluminium matrix composites. AdMSE. 2020;2020:3765791. doi: 10.1155/2020/3765791
[69] Balokhonov R, Romanova V, Kulkov A. Microstructure-based analysis of deformation and fracture in metal-matrix composite materials. Eng Fail Anal. 2020;110:104412. doi: 10.1016/J.ENGFAILANAL.2020.104412
[70] Sadeghi B, Cavaliere P. Reviewing the Integrated design approach for augmenting strength and toughness at macro- and micro-scale in high-performance advanced composites. Materials. 2023;16:5745. doi: 10.3390/MA16175745
[71] Wu W, Xia R, Qian G, et al. Mechanostructures: rational mechanical design, fabrication, performance evaluation, and industrial application of advanced structures. Prog Mater Sci. 2023;131:101021. doi: 10.1016/J.PMATSCI.2022.101021
[72] Rangrej S, Pandya S, Menghani J. Effects of reinforcement additions on properties of aluminium matrix composites – a review. Mater Today Proc. 2021;44:637–641. doi: 10.1016/J.MATPR.2020.10.604